引用格式：GUO Yun, CHEN Shenglin, WEI Xiangyu, et al. Temperature-insensitive Optical Fiber Tension Sensor Based on Vernier Effect[J]. Acta Photonica Sinica, 2022, 51(12):1206003
郭云,陈圣林,王平,等. 基于游标效应的温度不敏感光纤拉力传感器[J].光子学报,2022,51(12):1206003

基于游标效应的温度不敏感光纤拉力传感器

郭云[1],陈圣林[2],王平[1],魏翔宇[1],王玉娟[1],王善平[1],万海城[1]
(1 山东华宇工学院 电气工程学院,山东 德州 253000)
(2 德州职业技术学院 电子与新能源技术工程系,山东 德州 253000)

摘　要:提出了一种基于光学游标效应的并联法布里-珀罗干涉仪,实现了高灵敏度的光纤拉力传感。为实现高质量的游标效应,该传感器由两个法布里-珀罗干涉仪并联组成,分别为传感干涉仪和参考干涉仪,在此基础上,采用光纤衰减器来精确调控参考干涉仪的插入损耗,便于波长和强度之间的完美匹配。实验结果显示,并联后的拉力灵敏度达到了63.5 nm/N,线性度为99.26%,与单一传感干涉仪相比灵敏度提高了15.8倍。同时,温度串扰仅为9.8×10^{-4} N/℃。该传感器具备制作简单、灵敏度高、机械强度高、体积小以及成本低等优点,为恶劣条件下拉力测量提供了应用参考。

关键词:法布里-珀罗;并联;拉力;游标效应;高灵敏度;光纤衰减器
中图分类号:TN253　　**文献标识码**:A　　**doi**:10.3788/gzxb20225112.1206003

0　引言

光纤传感已经在生物医学[1]、健康监测[2]、人工智能[3]和环境监测等各个领域得到了广泛的应用。经过几十年的发展,各式各样的光纤传感相继被提出,其中有分布式光纤传感器[4]、光纤光栅传感器[1]、干涉型光纤传感器[5]。分布式光纤传感器适用于远距离测量,光纤光栅传感器测量灵敏度较低,显然干涉型光纤传感器在小范围、高灵敏度的需求中是更好的选择。常见干涉型光纤拉力传感器有马赫-曾德干涉仪(Mach-Zehnder Interferometer, MZI)[5]、法布里-珀罗干涉仪(Fabry-Perot Interferometer, FPI)[6]、萨格纳克干涉仪(Sagnak Interferometer, SI)[7]等。尽管干涉型传感器的灵敏度高于光纤光栅传感器,但有时不能够满足更高灵敏度的需求,因此近几年有学者提出了基于游标效应的级联型光纤干涉仪,其中包括双MZI级联[8]、双FPI级联[9]、MZI-FPI级联[10]等等。结构中的两个干涉仪,其中一个作为传感腔,另一个作为参考腔,这种方式可以将传感器的灵敏度放大几倍至十几倍,但级联结构的干涉腔长和插入损耗难以控制。2015年,QUAN Mingren等[11]提出一种基于光子晶体光纤的游标效应超高灵敏度开放腔的法布里-珀罗干涉仪气体折射率传感器,其灵敏度可达30 899 nm/RIU。2019年,ZHAO Yuxin等[12]制备了双FPI并联型全光纤液体折射率传感器,其折射率灵敏度达到了9 048.78 nm/RIU,放大了近8倍。2022年,SONG Xiaokang等[13]制备了双FPI并联型全光纤气体压力传感器,并联后结构的灵敏度比单一传感腔的灵敏度放大了11倍。相比与级联结构,该并联结构可分别对参考腔和和传感腔的长度进行精确切割,但能量匹配的问题仍未解决。因此,如何实现光纤内高质量的游标效应仍是亟待解决的问题。

本文提出了一种基于游标效应增敏的全光纤拉力传感器,该传感器由传感法布里-珀罗干涉仪(Sensing Fabry-Perot Interferometer, SFPI)和参考法布里-珀罗干涉仪(Reference Fabry-Perot Interferometer, RFPI)并联而成。通过光纤衰减器对RFPI能量的精确调节,实现了高质量的游标包络。同时,该传感器与单一SFPI相比,拉力灵敏度提高了15.8倍左右,且具有很好的抗温度干扰能力,温度串扰仅为9.8×10^{-4} N/℃。

基金项目:电气工程与智能控制协同创新中心(经费资助)
第一作者(通讯作者):郭云(1984—),女,副教授,硕士,主要研究方向为测量与检测、光纤传感等。Email:924313524@qq.com
收稿日期:2022-04-30;**录用日期**:2022-07-27

1 结构制备及其工作原理

传感器的结构示意图如图1所示，其中SFPI通过法兰盘连接在光纤耦合器的3接口处，RFPI与光纤耦合器的4接口之间串联光纤衰减器(Attenuator)，SFPI与RFPI组成并联结构。

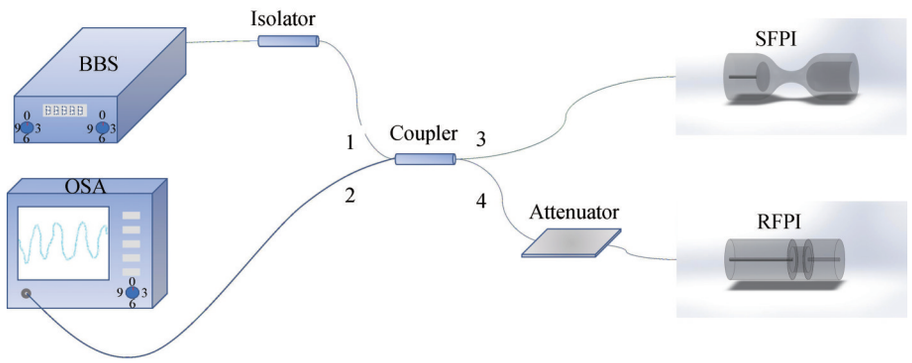

图1 试验系统示意图

Fig.1 Test system schematic diagram

RFPI为开放的空气腔，其具体的制备方法为：1)将一段特定长度的内径为80 μm的空芯光纤(Polymicro Technologies，TSP080125)的一端熔接在单模光纤(康宁SMF28)上，如图2(a)所示；2)在电荷藕合器件(Charge Coupled Device，CCD)的辅助下精确控制所需长度，并将多余的内径为80μm的空芯光纤进行切除，如图2(b)所示；3)将步骤2中预制结构的空芯光纤一端与内径为10 μm的空芯光纤(Polymicro Technologies，TSP010125)相熔接，如图2(c)所示。

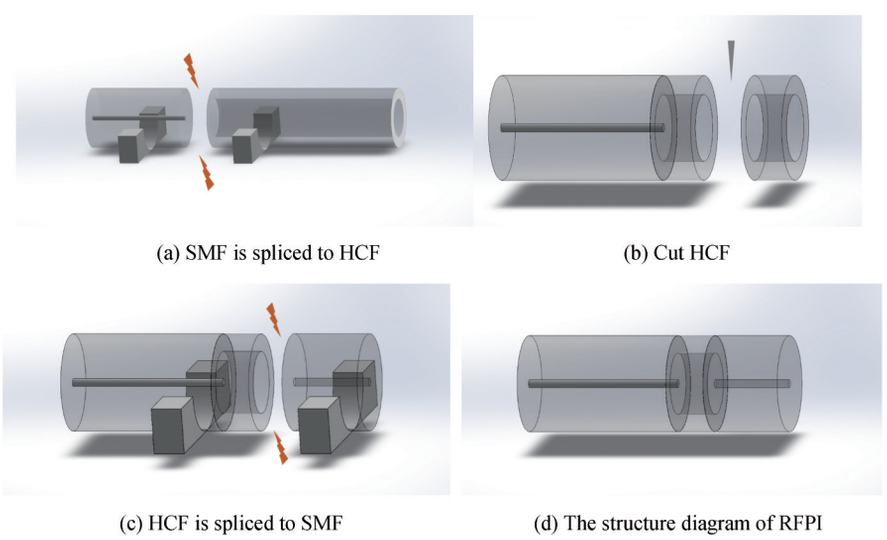

图2 RFPI制备示意图

Fig.2 RFPI preparation of schematic diagram

SFPI为封闭的空气腔，其具体的制备方法为：1)将一段单模光纤与一段内径为80 μm的空芯光纤熔接，作为预制光纤，如图3(a)所示；2)设置熔接机放电强度为10 bit，放电时间为700 ms，使其处于偏拉锥状态；3)通过控制熔接机夹具的位移，使预制光纤移动至熔接点偏离放电针一定距离后，在空芯光纤上进行放电，使空芯光纤塌陷形成封闭腔，如图3(c)～(d)所示。该步骤能够通过控制熔接机夹具的位移，从而精准控制封闭腔的长度；4)减小熔接机的放电强度为8 bit，对步骤3中制备的封闭腔进行多次放电，使封闭腔内部的反射面光滑无瑕疵，从而提高反射光功率。

由图1所示，RFPI和SFPI的反射面两侧介质均分别为空气和二氧化硅，因此各反射面的反射率可由式(1)求出

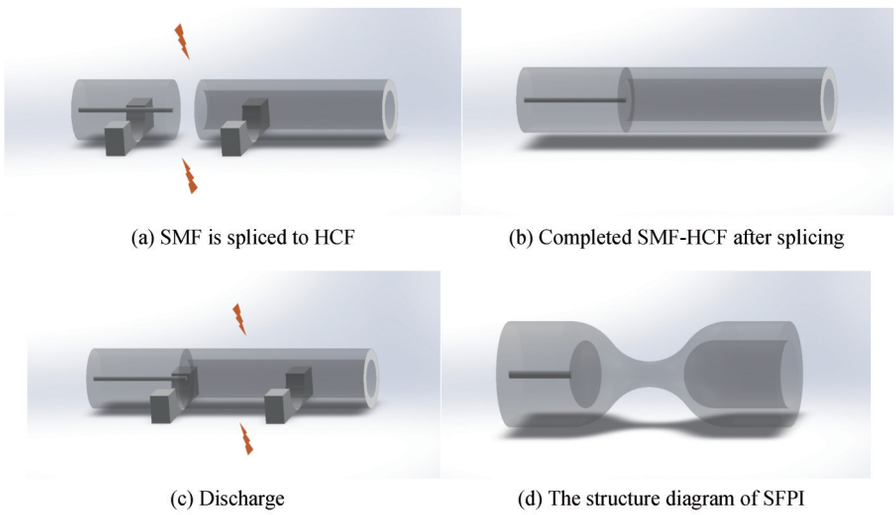

图3　SFPI制备示意图

Fig.3　SFPI preparation of schematic diagram

$$R=\frac{\left(n_c-n_1\right)^2}{\left(n_c+n_1\right)^2} \tag{1}$$

式中，R为反射率，$n_c=1$和$n_1=1.45$分别为空气和二氧化硅的有效折射率，可计算得出反射面的反射率大约为3.5%。因其反射率较低，高阶反射光的能力弱，几乎可以忽略不计，因此可近似为双光束干涉。SFPI和RFPI的反射光强I_S和I_R分别为[6]

$$I_S=I_1+I_2+2\sqrt{I_1I_2}\cos\left(\frac{4n_cL_1}{\lambda}+\phi_0\right) \tag{2}$$

$$I_R=I_3+I_4+2\sqrt{I_3I_4}\cos\left(\frac{4n_cL_2}{\lambda}+\phi_1\right) \tag{3}$$

式中，I_1和I_2分别表示SFPI两个反射面的反射光强，L_1为SFPI空气腔的长度，λ为共振波长，φ_0和φ_1分别为SFPI和RFPI的初相，I_3和I_4分别表示RFPI两个反射面的反射光强，L_2为RFPI空气腔的长度。当满足$(4nL)/\lambda+\varphi=(2m+1)\pi(m=0,1,2\cdots)$时，出现干涉条纹。此时对应的干涉谷的波长为

$$\lambda=\frac{2n_cL}{2m+1} \tag{4}$$

由式(4)，可以看出单一干涉条纹波长λ随着腔长L的增加而增加，即发生红移。SFPI和RFPI通过光纤耦合器并联后，两束光的合成光强I_r为[12]

$$I_r=E+2a\cos\frac{4n_c(L_1-L_2)\pi}{\lambda} \tag{5}$$

式中，E为常数，a为包络的振幅。由于SFPI和RFPI干涉条纹上的各个极值点的合成可以产生具有周期性包络的光谱。包络曲线的函数式可由$\partial I_r/\partial\lambda=0$求导得出

$$F_C=D+2m\cos\left[\frac{4\pi(h_1-h_2)}{\lambda}\right] \tag{6}$$

式中，D为函数的直流部分，m为函数交流部分的振幅，h_1和h_2分别表示SFPI和RFPI的光程。则包络函数的自由光谱范围(Free Spectral Range，FSR)为

$$\mathrm{FSR_C}=\frac{\mathrm{FSR_1}\cdot\mathrm{FSR_2}}{\left|\mathrm{FSR_1}-\mathrm{FSR_2}\right|} \tag{7}$$

本文提出的传感器仅SFPI参与拉力的测量，因此光程h_2为常数，h_1随着拉力的变化而变化，则相应的FSR为

$$\mathrm{FSR}_1=\frac{\lambda_1\lambda_2}{2h_1}=\frac{\lambda_1\lambda_2}{2nL_1} \tag{8}$$

SFPI的拉力灵敏度和包络函数的拉力灵敏度可分别表示为[14]

$$S_{\mathrm{F-single}}=\frac{\partial\lambda_N}{\partial F}=\lambda_N\left(\frac{\partial L_1}{\partial F}\frac{1}{L_1}+\frac{\partial n}{\partial F}\frac{1}{n}\right) \tag{9}$$

$$S_{\mathrm{F-envnlope}}=\frac{\partial\lambda}{\partial F} \tag{10}$$

结合式(6)、(8)和(10)可推导出包络曲线波谷中心波长的拉力灵敏度为

$$S_{\mathrm{F-envnlope}}=\lambda_N\left(\frac{\partial L_1}{\partial F}\frac{1}{L_1}+\frac{\partial n}{\partial F}\frac{1}{n}\right)\frac{\mathrm{FSR}_1}{\left|\mathrm{FSR}_1-\mathrm{FSR}_2\right|} \tag{11}$$

式(11)与式(9)相比,包络曲线的拉力灵敏度比SFPI的拉力灵敏度放大了M倍。其中M的大小结合式(9)和(11)可得

$$M=\left|\frac{S_{\mathrm{F-envnlope}}}{S_{\mathrm{F-single}}}\right|=\frac{\mathrm{FSR}_1}{\left|\mathrm{FSR}_1-\mathrm{FSR}_2\right|} \tag{12}$$

为形成高质量的游标包络,在RFPI与光纤耦合器之间加入光纤衰减器来调控RFPI的插入损耗使其和SFPI的能量相匹配,并通过数值分析法和实验验证了光纤衰减器对游标包络质量的影响,仿真和实验结果如图4所示。

由图4(a)可知SFPI与RFPI的插入损耗不一致时,游标包络的对比度为0.36,而当加入光纤衰减器使

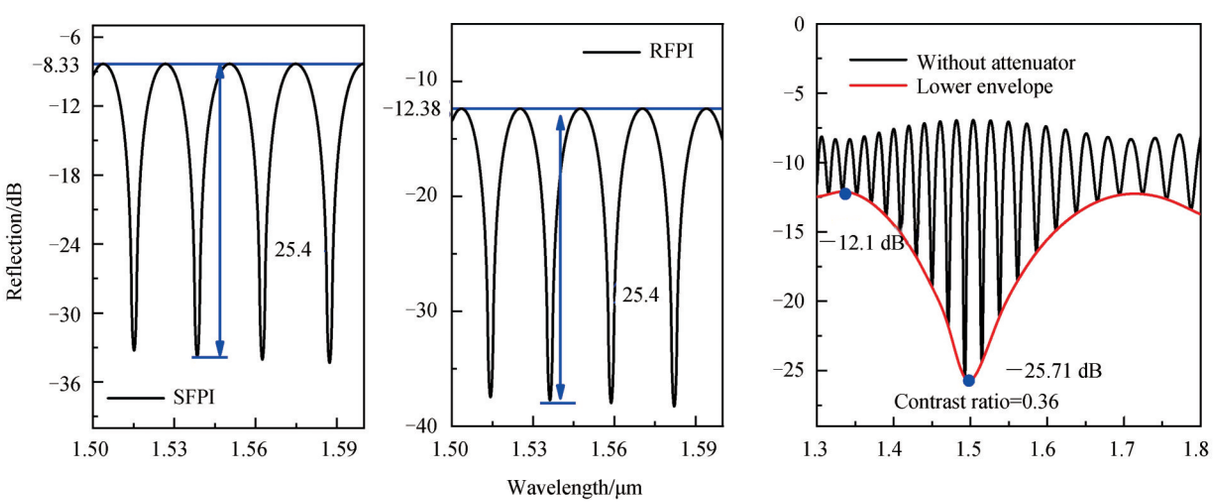

(a) Without attenuator (simulation)

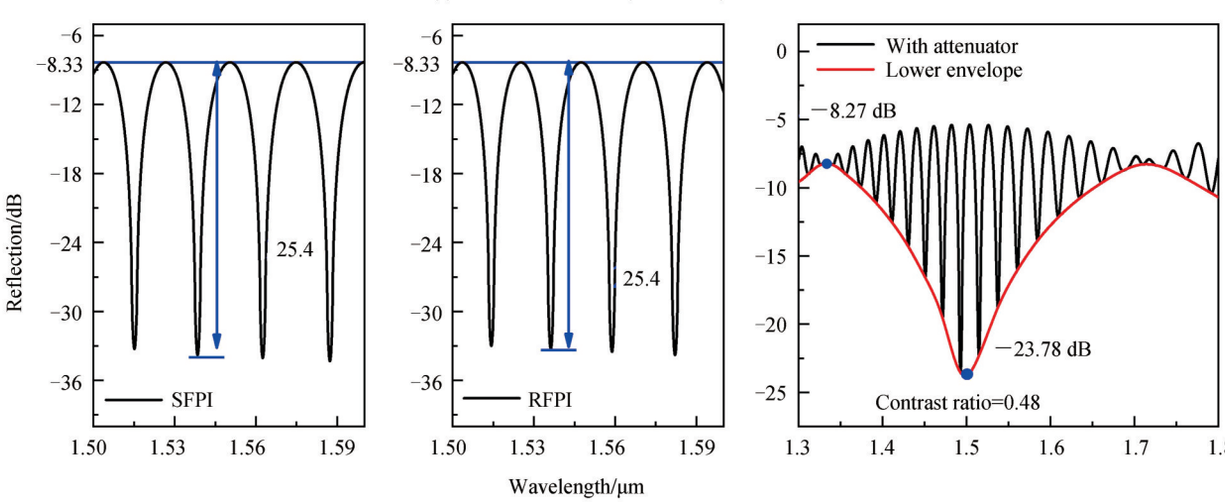

(b) With attenuator (simulation)

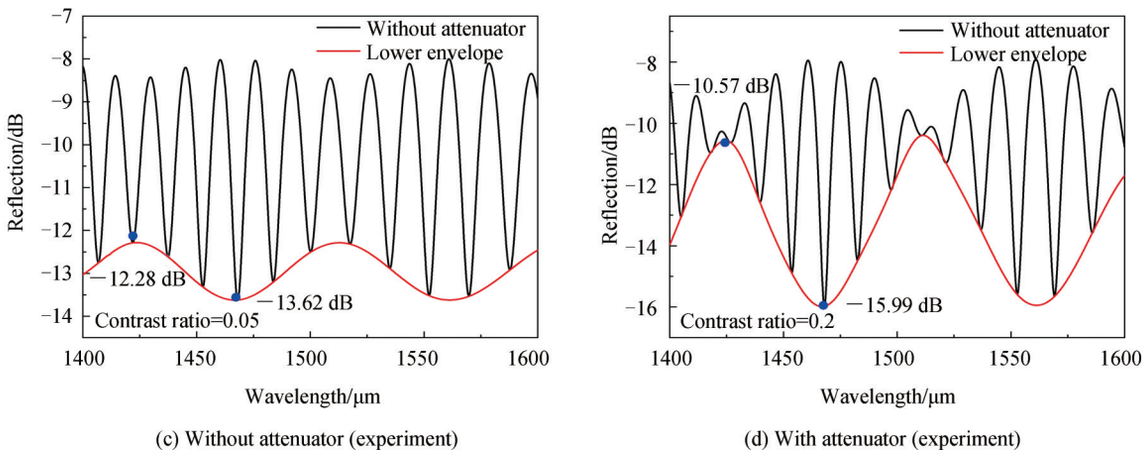

图4　有无衰减器的叠加光谱对比

Fig.4　Attenuator function simulation

SFPI和RFPI的插入损耗一至时，游标包络的对比度提升至0.48，由图4(b)可得。通过图4(c)～(d)可得，在实验条件下加入光纤衰减器前后，包络的对比度由0.05提升至0.2。因此加入光纤衰减器能够有效的提升游标包络的质量。该结构因其独特的空芯光纤级联结构可满足实际应用中的多功能化的需求，能实现高灵敏度的拉力、压强同步测量[15-16]。

2　实验结果及分析

实验系统如图5所示，宽带光源(Broadband light Source，BBS，1 400～1 600 nm)发出的信号光首先经隔离器通过光纤耦合器进入SFPI和RFPI，经SFPI和RFPI干涉后反射进入的光纤耦合器进行合成，最终进入光谱分析仪(optical spectrum analyzers，OSA，分辨率0.02 nm)。通过在SFPI末端添加不同质量的砝码进行拉力的测量，SFPI末端预留足够长的SMF，并在SMF的尾端粘连挂钩，用于悬挂不同质量的砝码。需要注意的是，因挂钩和光纤自身存在质量，因此在实验测量之前要保证光纤和挂钩处于稳定状态时作为无拉力状态。

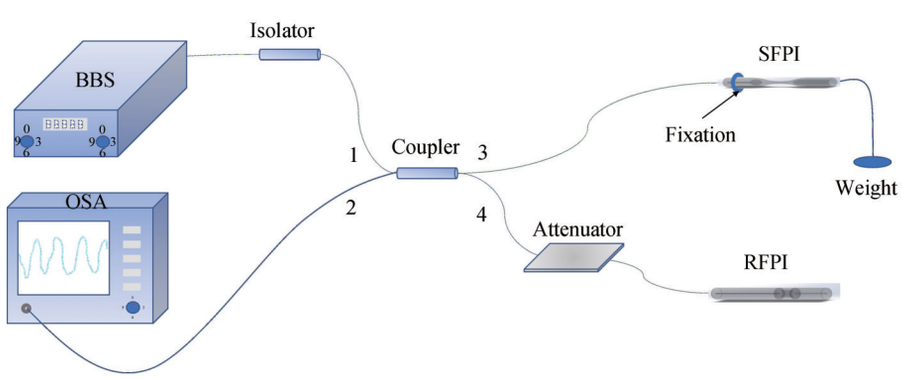

图5　并联FPI传感器的实验系统

Fig. 5　Experimental system for paralleled FPI sensor

本次实验制备的SFPI的腔长L_1=67 μm。首先对单一SFPI进行拉力测试，实验结果如图6所示。

通过图6(a)可以看出，随着拉力的增加，引起腔长的增加，SFPI的干涉条纹发生红移现象，与式(4)中的分析一致，对应的增大拉力灵敏度为4.022 nm/N，减小拉力灵敏度为3.986 nm/N，线性度均为0.999，加减拉力灵敏度相差仅为0.036 nm/N，因此该传感器具有较好的重复性。

为了进一步提升传感器的拉力灵敏度，本次实验分别制备了两个RFPI，其腔长分别为L_2=80 μm和L_3=63 μm，并分别与SFPI组成并联结构一和并联结构二。对两组并联结构进行了拉力实验，实验结果如图7所示。

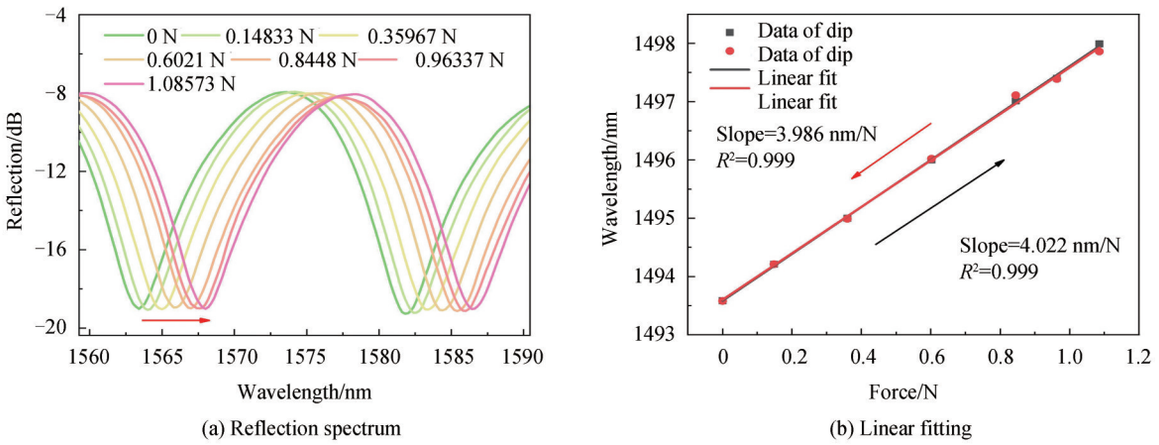

(a) Reflection spectrum　　(b) Linear fitting

图 6　单个 SFPI 的拉力响应

Fig. 6　Tension response of single SFPI

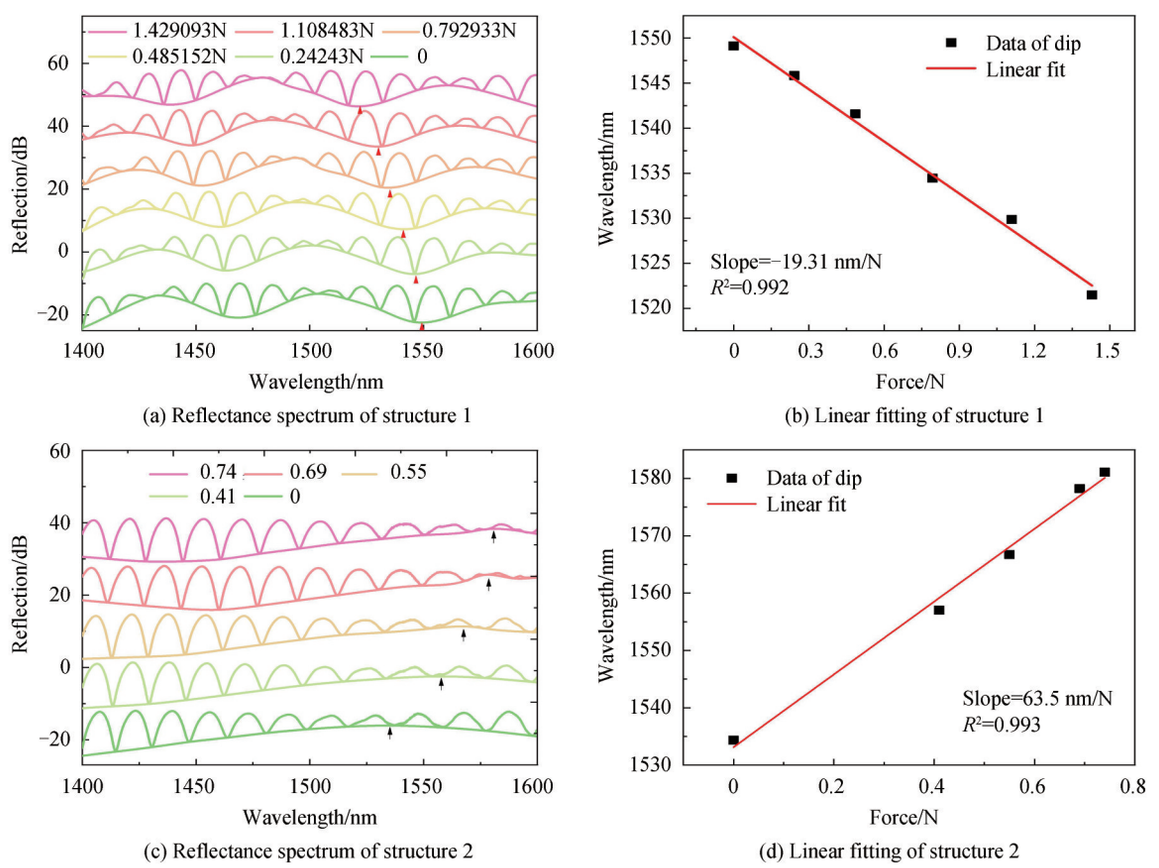

(a) Reflectance spectrum of structure 1　　(b) Linear fitting of structure 1

(c) Reflectance spectrum of structure 2　　(d) Linear fitting of structure 2

图 7　并联 FPI 传感器对拉力的响应

Fig.7　Response of paralleled FPI sensor to tension

如图 7(a)～(b)所示，随着拉力的增加，结构一的反射光谱发生了明显的蓝移。对应的拉力灵敏度为−19.31 nm/N，线性度为 0.992，与单一 SFPI 的灵敏度相比，放大了 4.8 倍。如图 7(c)～(d)所示，随着拉力的增加，结构二的反射光谱发生了明显的红移，对应的拉力灵敏度为 63.5 nm/N，线性度为 0.993，与单一 SFPI 的灵敏度相比，放大了 15.8 倍，与理论分析一致。与先前报道的部分拉力传感器相比灵敏度有显著的提升，如表 1 所示。本次实验获得了几倍至十几倍的灵敏放大，并利用光纤衰减器使 SFPI 和 RFPI 的能量相匹配，获得了较好的游标包络，提高了测量精度。

表1　与先前报道文献的传感器性能对比分析

Table 1　Performance analysis of the proposed probe with that reported in literature

Type of probe	Force sensitivity	Reference
Microcavity spliced with SMF-HCF(Orb)-SMF	0.75 nm/N	[17]
Microcavity spliced with SMF-HCF-SMF	14.2 nm/N	[18]
Microcavity spliced with SMF-HCF(Orb)	3.73 nm/N	[19]
Proposed probe	63.5 nm/N	Our sensor

本文提出的基于光学游标效应的并联FPI不仅具有较高的拉力灵敏度，其游标包络也具有较高的稳定性。为了验证游标包络的稳定性，对结构一进行了游标包络稳定性实验，相同拉力条件下每隔2 min取一点，共取五个点。实验结果如图8所示。由图8可得，游标包络在不改变拉力的情况下的最大漂移量$\Delta\lambda$=0.02 nm。因此该传感器具有良好的稳定性。

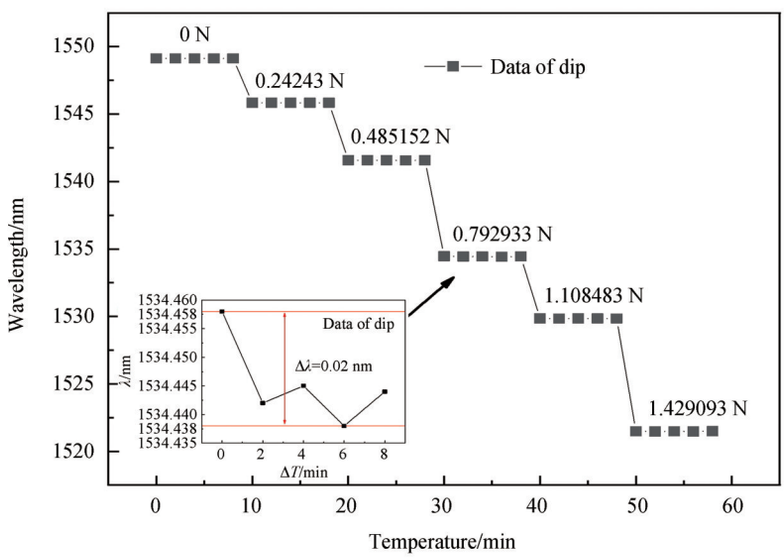

图8　游标包络稳性响应

Fig.8　Vernier envelope stability response

因光纤本身具有热光效应和热膨胀效应，因此存在着温度串扰，为了探究传感器的温度串扰，本文进行了单一SFPI和并联结构一的温度实验，温度测量范围为100～600 ℃，每隔100 ℃取一点，实验结果如图9所示。由图9可得，单一SFPI和并联结构一的温度灵敏度分别为3.93 pm/℃和－18.91 pm/℃，单一SFPI与并联结构一的灵敏度相比，后者放大了约4.8倍，这是因为RFPI腔为开放腔，且其中的介质为空气，空气的热光系数和热膨胀系数较低，因此对温度响应不敏感[14]。实验结果表明该结构的传感器温度串扰仅为

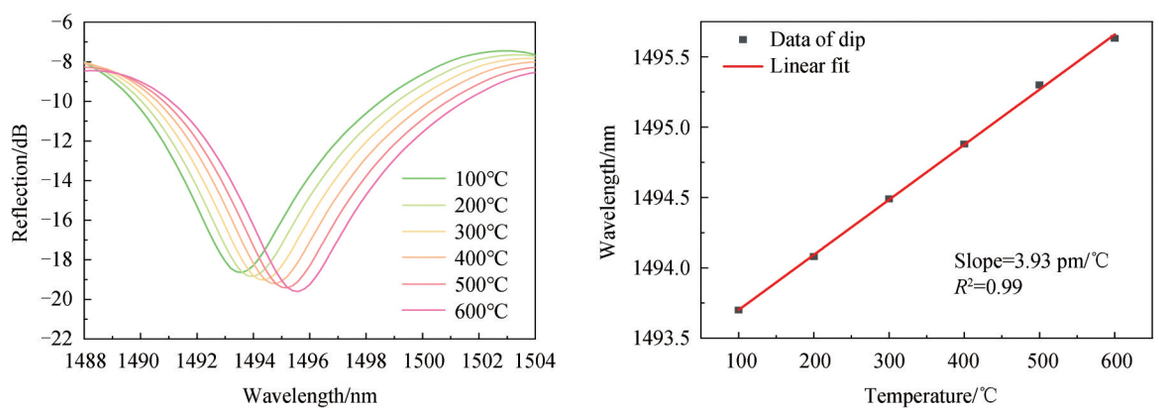

(a) Temperature response of single SFPI　　(b) Linear fit of SFPI

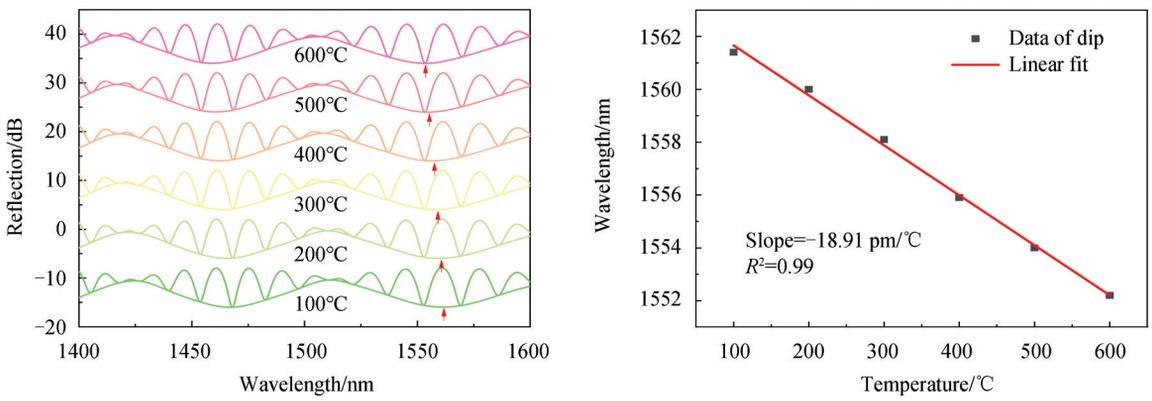

(c) Reflection spectrum under different temperature　　(d) Linear fit of parallel

图 9　传感器的温度响应

Fig.9　Temperature test of the sensor

9.8×10^{-4} N/℃，因此该传感器可满足高温环境下的拉力测试。

为了验证实验数据的可靠性和真实性，结合实验参数和式(5)，进行了两组理论模拟。式(5)内的参数设置分别为：根据实际情况计算得出反射面的反射率约为0.035，即$R_1=R_2=R_3=R_4=0.035$；又因为两个F-P腔内均以空气为传光介质，所以$n_c=1$；第一组理论模拟的RFPI的腔长$L_2=80$ μm，SFPI的腔长$L_1=67$ μm（$L_1<L_2$）；第二组理论模拟的RFPI的腔长$L_3=63$ μm，SFPI的腔长$L_1=67$ μm（$L_1>L_3$）；改变SFPI的腔长模拟拉力变化，RFPI不参加拉力测试，理论模拟结果如图10所示。

由图10(a)～(c)可以看出，当SFPI腔长小于RFPI腔长时，随着拉力的增加，包络线的飘移方向与单一SFPI干涉谱的飘移方向相反，并且实现了4.99倍的放大。由图10(d)～(f)可以看出当SFPI腔长大于RFPI

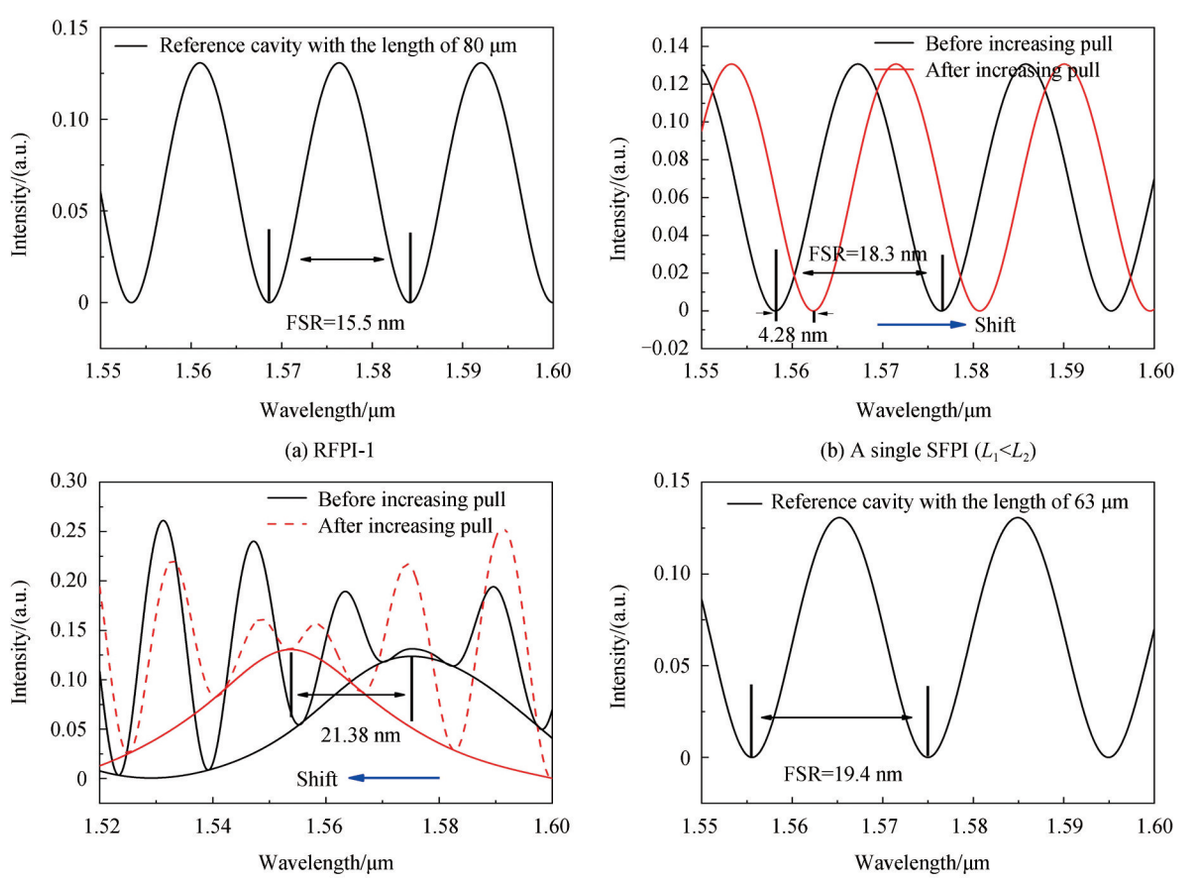

(a) RFPI-1　　(b) A single SFPI ($L_1<L_2$)

(c) Spectrum of RFPI-1 and SFPI in parallel　　(d) RFPI-2

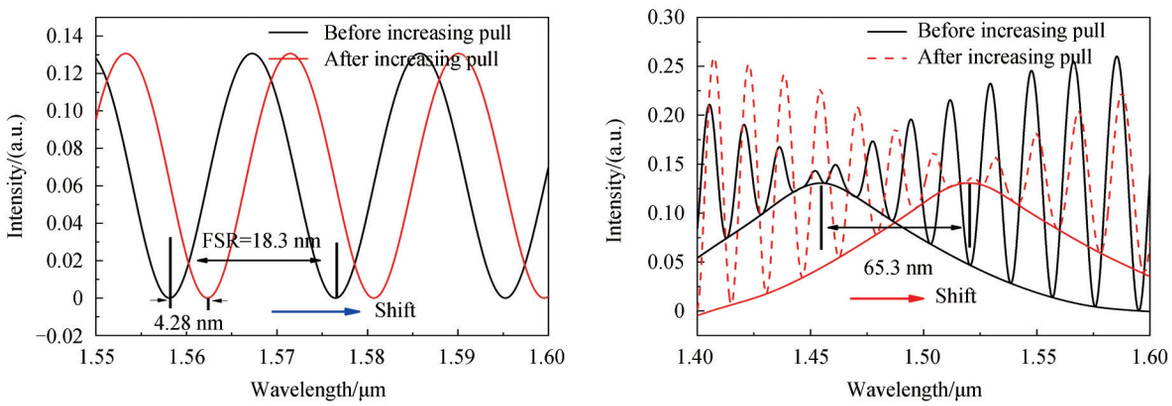

(e) A single SFPI (L_1>L_3)　　(f) Spectrum of RFPI-2 and SFPI in parallel

图 10　模拟拉力响应波长偏移

Fig. 10　Simulated wavelength shift of tension response

腔长时，随着拉力的增加，包络线的飘移方向与单一SFPI干涉谱的飘移方向一致，并且实现了15.26倍的放大。理论模拟结果与实验结果基本一致，误差小于0.04，对于该误差出现的原因，经分析可能有以下几种：1）理论模拟种默认腔内气体折射率为1，与实际有一定的误差；2）实验数据线性拟合未达到100%，存在一定的误差；3）实验设备本身存在的误差。本文同时对相同SFPI时，不同RFPI腔长对放大倍数的影响进行了理论仿真分析，分析结果得出RFPI的腔长与SFPI的腔长差值越小，放大倍数越大，与式（12）相对应。结果如图11所示。

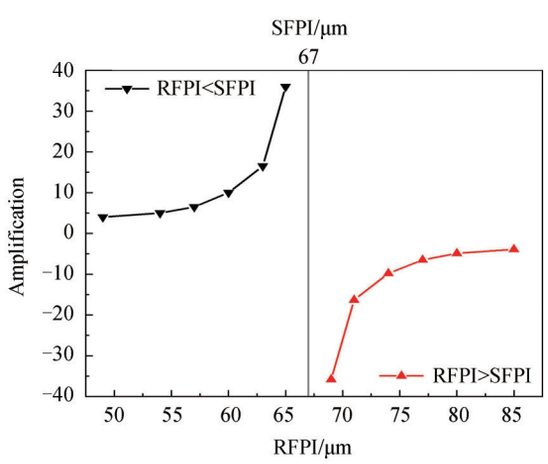

图 11　不同腔长的RFPI对放大倍数的影响

Fig.11　Effect of RFPI of different cavity lengths on magnification

3　结论

本文提出了一种基于并联FPI产生游标效应的高灵敏度光纤高温拉力传感器。拉力灵敏度可从4.022 nm/N提高到63.5 nm/N，放大系数为15.8，相应的线性度为0.993。同时，该传感器在100～600 ℃范围内的温度串扰仅为9.8×10^{-4} N/℃，因此该传感器能很好的抵御温度波动带来的影响。并通过加入光纤衰减器来调节SFPI和RFPI之间的能量配比，实现了高质量的游标包络。此外，因该传感器参考腔的特殊结构，有望实现同一传感器功能化的集成。

参考文献

[1]　GUO Tuan. Review on plasmonic optical fiber grating biosensors[J]. Acta Optica Sinica, 2018, 38(3): 0328006.
郭团. 等离子体共振光纤光栅生物传感器综述[J]. 光学学报, 2018, 38(3): 0328006.

[2]　STEPHENS A, BUSCH A, SALAMONSEN R, et al. A novel fibre Bragg grating pressure sensor for rotary ventricular

assist devices[J]. Sensors and Actuators A: Physical, 2019, 295: 474-482.
[3] SCHENATO L, RONG Qiangzhou, SHAO Zhihua, et al. Highly sensitive FBG pressure sensor based on a 3D-printed transducer[J]. Journal of Lightwave Technology, 2019, 37(18): 4784-4790.
[4] WANG Huaping. Influence of interfacial effect between distributed optical fiber sensors and monitored structures[J]. Acta Optica Sinica, 2022, 42(2): 0206004.
王花平. 分布式光纤传感器与被测结构的界面效应影响分析[J]. 光学学报, 2022, 42(2): 0206004.
[5] HOU Liangtao, ZHANG Xudong, YANG Jiuru, et al. Simultaneous measurement of refractive index and temperature based on half-tapered SMS fiber structure with fringe-visibility difference demodulation method [J]. Optics Communications, 2019, 433: 252-255.
[6] WEI Xiangyu, SONG Xiaokang, LI Cang, et al. Optical fiber gas pressure sensor based on Polydimethylsiloxane microcavity[J]. IEEE Journal of Lightwave Technology, 2021, 39(9): 2988-2993.
[7] ZHAO Xinqiu, ZHENG Shengxuan, HAN Peifu. Application of fiber-optic Sagnac interferometer in strain sensor[J]. Laser and Infrared, 2004, 34(2): 147-148.
赵新秋,郑绳楦,韩佩富. 光纤萨格纳克干涉仪在应变传感器中的应用[J]. 激光与红外, 2004, 34(2): 147-148.
[8] LIAO Hao, LU Ping, FU Xin, et al. Sensitivity amplification of fiber-optic in-line Mach-Zehnder Interferometer sensors with modified Vernier-effect[J]. Optics Express, 2017, 25(22): 26898-26909.
[9] LI Zhe, ZHANG Yanxin, ZHANG Weigang, et al. High-sensitivity gas pressure Fabry - Perot fiber probe with micro-channel based on vernier effect[J]. Journal of Lightwave Technology, 2019, 37(14):3444-3451.
[10] LI Jiewen, ZHANG Meng, WAN Minggui, et al. An ultrasensitive refractive index sensor based on enhanced vernier effect through cascaded fiber core-offset pairs[J]. Optics Express, 2020, 28(3): 4145-4155.
[11] QUAN Mingren, TIAN Jiajun, YAO Yong. Ultra-high sensitivity Fabry-Perot interferometer gas refractive index fiber sensor based on photonic crystal fiber and Vernier effect[J]. Optics Letters, 2015, 40(21): 4891-4894.
[12] ZHAO Yuxin, JIANG Jiuxing, YANG Yuqiang, et al. A sensitivity-enhanced all-fiber optic liquid refractive index sensor based on vernier effect[J]. Acta Optica sinica, 2019, 48(11): 1148022.
赵玉欣,姜久兴,杨玉强,等. 基于游标效应增敏的全光纤液体折射率传感器[J]. 光子学报, 2019, 48(11): 1148022.
[13] SONG Xiaokang, HOU Liangtao, WEI Xiangyu, et al. High sensitivity fiber gas pressure sensor with two separated Fabry-Pérot interferometers based on the vernier effect[J]. Photonics, 2022, 9(1): 31.
[14] WEI Xiangyu. Fabry-perot interferometric fiber optic microcavity pressure sensor[D]. Harbin: Heilongjiang University, 2021.
魏翔宇. 法布里-珀罗干涉型光纤微腔压强传感器[D]. 哈尔滨:黑龙江大学, 2021.
[15] HE Haoyang, LIU Yi, LIAO Yingying, et al. Simple fiber-optic sensor for simultaneous and sensitive measurement of high pressure and high temperature based on the silica capillary tube[J]. Optics Express, 2019, 27(18): 25777-25788.
[16] XU Ben, WANG Chao, WANG Dongning, et al. Fiber-tip gas pressure sensor based on dual capillaries[J]. Optics Express, 2015, 23(18): 23484-23492.
[17] ZHAO Yong, XIA Feng, CHEN Maoqing, et al. Optical fiber axial contact force sensor based on bubble-expanded Fabry - Pérot interferometer[J]. Sensors and Actuators A Physical, 2018, 272: 318-324.
[18] DASH J, LIU Zhenyong, GUNAWARDENA D S, et al. Fabry-Perot cavity-based contact force sensor with high precision and a broad operational range[J]. Optics Letters, 2018, 44(14):3546-3549.
[19] YI Guo, GUO Ying, ZHANG Yundong. Zero cross-sensitive tip thin-walled FPIs based on stretch and arc micromachining technology for lateral load applications[J]. Measurement Science and Technology, 2021, 32(10): 105113-105119.

Temperature-insensitive Optical Fiber Tension Sensor Based on Vernier Effect

GUO Yun[1], CHEN Shenglin[2], WANG Ping[1], WEI Xiangyu[1], WANG Yujuan[1], WANG Shanping[1], WAN Haicheng[1]

(1 *School of Electrical Engineering, Shandong Huayu Institute of Technology, Dezhou, Shandong* 253000, *China*)

(2 *Department of Electronics and New Energy Technology Engineering, Texas Vocational and Technical College, Dezhou, Shandong* 253000, *China*)

Abstract: Based on distributed fiber optic sensors, fiber grating sensors and fiber interferometers have been widely used in tensile force measurement. In contrast, fiber interferometers have been widely studied due to their high sensitivity, such as Mach-Zehnder Interferometers (MZI), Fabry-Perot Interferometers (FPI), and Sagnac Interferometers (SI). On this basis, in order to improve the tensile force sensitivity of fiber interferometers, cascade fiber interferometers based on Vernier effect are proposed, such as cascaded dual MZI, cascaded dual FPI and cascaded MZI-FPI structures. However, the matching of the optical path difference and insertion loss of the cascade structure has always been a difficult problem to solve, which can affect the spectral quality of the Vernier effect. Therefore, the sensing accuracy and resolution of the tensile force measurements are limited. In this paper, a parallel FPI all-fiber tensile force sensor based on the Vernier effect is proposed, which is composed of a Sensing FPI (SFPI) and a Reference FPI (RFPI) in parallel. The structure is prepared only by an arc discharge technology, which ensures the uniformity and repeatability of the structure preparation. Among them, the SFPI is a closed air cavity. The tapered air microcavity is fabricated by precisely controlling the discharge position of HCF by an optical fiber fusion splicer. Then, the tapered air microcavity is discharged multiple times with a small current to improve the reflectivity of the microcavity. RFPI is an open air cavity. A section of HCF and Single-Mode Fiber (SMF) with an inner diameter of 80 μm is directly fused, and the length of the HCF cavity is precisely controlled by a precision cutting platform, so that the FSR of the interference spectrum is consistent with the SFPI. Subsequently, a section of HCF with an inner diameter of 10 μm is splicing on the end face. The parallel structure only consists of SMF and HCF, and the thermal expansion coefficient and thermo-optic coefficient of silica and air are very small, which reduces the crosstalk effect of temperature on tensile force. Through theoretical analysis, it is found that when the optical path difference between SFPI and RFPI is close to when not equal, a Vernier effect can be formed, and the smaller the optical path difference ratio between the two, the greater the sensitivity magnification. In order to form a high-quality Vernier envelope, a fiber attenuator is added between the RFPI and the fiber coupler to adjust the insertion loss of the RFPI to match the energy of the SFPI. The influence of the fiber attenuator on the Vernier envelope quality is verified by numerical analysis and experiments. The experimental results show that after adding the fiber attenuator, the contrast ratio of the Vernier envelope is increased from 0.05 to 0.2, and the magnification is four times. In the experiment, SFPI with a cavity length of 67 μm is prepared for tensile force test. In order to verify the hysteresis of the tensile force sensor, the experiments of increasing and decreasing the tensile force are carried out, respectively, with the sensitivities of 4.022 nm/N and 3.986 nm/N. In order to further increase the tensile force sensitivity of the sensor, two RFPIs with cavity lengths of 80 μm and 63 μm are prepared in this experiment, and formed parallel structure 1 and parallel structure 2 with SFPI, respectively. Tensile force experiments are carried out on two groups of parallel structures. With the increase of tensile force, the reflection spectrum of structure 1 undergoes a clear blue-shift. The corresponding sensitivity is −19.31 nm/N with the linearity of 0.992, which is 4.8 times larger than the sensitivity of a single SFPI. With the increase of tensile force, the reflection spectrum of structure 2 undergoes an obvious red-shift. The corresponding tensile force sensitivity is 63.5 nm/N with the linearity of 0.993, which is 15.8 times larger than the sensitivity of a single SFPI. The simulation analysis shows that when the SFPI cavity length is greater than the RFPI cavity length, with the increase of the tensile force, the drift direction of the envelope is consistent with the drift direction of the single SFPI interference spectrum. To explore the temperature crosstalk of the sensors, the temperature experiment of single SFPI and parallel structure 1 is carried out, and the temperature measurement range is 100℃ ~600 ℃. The experimental results show that the temperature sensitivity of single SFPI and parallel structure 1 are

3.93 pm/°C and −18.91 pm/°C, respectively, the sensitivity is amplified by about 4.8 times, and the temperature crosstalk is only 9.8×10^{-4} N/°C. To verify the stability of the proposed sensor, structure 1 is tested under different tensile force conditions. The experimental results show that the maximum drift of the Vernier envelope at 0.79 N is 0.02 nm, which proves that the sensor has good stability. In this paper, a high-sensitivity fiber-optic tensile force sensor based on the Vernier effect is proposed, which consists of a parallel FPI structure. By matching the energies of SFPI and RFPI through fiber attenuators, the Vernier envelope quality is optimized. The tensile force sensitivity can be improved from 4.022 nm/N to 63.5 nm/N, and the amplification factor is 15.8 with the linearity of 0.993. The simulation results show that the experimental results are basically consistent with the theory. At the same time, the temperature crosstalk of the sensor in the range of 100°C ~600 °C is only 9.8×10^{-4} N/°C.

Key words: Fabry-Perot; Paralleled; Tension; Vernier effect; High sensitivity; Fibre optic attenuator
OCIS Codes: 060.2370; 120.2230; 120.6710; 280.4788

Foundation item: Electrical Engineering and Intelligent Control Collaborative Innovation Center (Funded)